J. Fluid Mech. (2024), *vol*. 978, A5, doi:10.1017/jfm.2023.1004

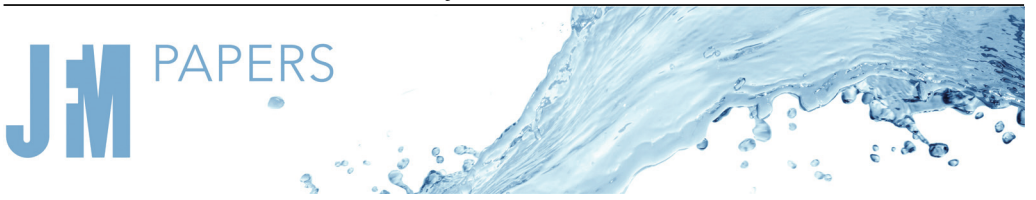

Revealing the mechanism and scaling laws behind equilibrium altitudes of near-ground pitching hydrofoils

Tianjun Han[1,†], **Qiang Zhong**[2,3], **Amin Mivehchi**[1], **Daniel B. Quinn**[2,4] and **Keith W. Moored**[1]

[1]Department of Mechanical Engineering and Mechanics, Lehigh University, Bethlehem, PA 18015, USA

[2]Department of Mechanical and Aerospace Engineering, University of Virginia, Charlottesville, VA 22904, USA

[3]Department of Mechanical Engineering, Iowa State University, Ames, IA 50011, USA

[4]Department of Electrical and Computer Engineering, University of Virginia, Charlottesville, VA 22904, USA

(Received 27 April 2023; revised 5 October 2023; accepted 19 November 2023)

A classic lift decomposition (Von Kármán & Sears, *J. Aeronaut. Sci.*, vol. 5, 1938, pp. 379–390) is conducted on potential flow simulations of a near-ground pitching hydrofoil. It is discovered that previously observed stable and unstable equilibrium altitudes are generated by a balance between positive wake-induced lift and negative quasi-steady lift while the added mass lift does not play a role. Using both simulations and experiments, detailed analyses of each lift component's near-ground behaviour provide further physical insights. When applied to three-dimensional pitching hydrofoils the lift decomposition reveals that the disappearance of equilibrium altitudes for $\mathcal{R}$ (aspect ratio) < 1.5 occurs due to the magnitude of the quasi-steady lift outweighing the magnitude of the wake-induced lift at all ground distances. Scaling laws for the quasi-steady lift, wake-induced lift and the stable equilibrium altitude are discovered. A simple scaling law for the lift of a steady foil in ground effect is derived. This scaling shows that both circulation enhancement and the velocity induced at a foil's leading edge by the bound vortex of its ground image foil are the essential physics to understand steady ground effect. The scaling laws for unsteady pitching foils can predict the equilibrium altitude to within 20 % of its value when St (Strouhal number) < 0.45. For $St \geq 0.45$ there is a wake instability effect, not accounted for in the scaling relations, that significantly alters the wake-induced lift. These results not only provide key physical insights and scaling laws for steady and unsteady ground effects, but also for two schooling hydrofoils in a side-by-side formation with an out-of-phase synchronization.

Key words: propulsion, swimming/flying

† Email address for correspondence: tih216@lehigh.edu

1. Introduction

Many animals improve their locomotion energetics or increase their range by swimming or flying near the seafloor or water surface, thereby taking advantage of ground effect (Baudinette & Schmidt-Nielsen 1974; Blake 1979; Hainsworth 1988; Webb 1993, 2002; Park & Choi 2010). When wings/fins move steadily near a boundary, such as those of gliding animals or fixed-wing aircraft, it is well-known that a steady ground effect increases their lift and reduces their induced drag (Widnall & Barrows 1970; Yang, Yang & Li 2009; Boschetti *et al.* 2010; Yang, Lin & Yang 2010; Lee & Lee 2011; He, Qu & Agarwal 2015; Qu *et al.* 2015; Tremblay Dionne & Lee 2018; Baddoo *et al.* 2020). However, when swimmers or flyers oscillate their appendages near a boundary, like flatfish swimming near the ocean floor, they experience an unsteady ground effect.

Unsteady ground effect produces a host of hydrodynamic phenomena. For example, foils oscillating near a boundary experience a thrust or cruising speed enhancement with no penalty to their propulsive efficiency (Tandida 2001; Iosilevskii 2008; Quinn, Lauder & Smits 2014*a*; Wu *et al.* 2014; Fernández-Prats *et al.* 2015; Dai, He & Zhang 2016; Park, Kim & Sunga 2017), and vortex wakes are deflected near boundaries due to their image vortices (Quinn *et al.* 2014*b*; Kurt *et al.* 2019; Zhong *et al.* 2019). Moreover, stable equilibrium altitudes arise where an increase/decrease in a swimmer's altitude causes a negative/positive lift force, pulling the swimmer back to a stable altitude (Quinn *et al.* 2014*b*; Mivehchi, Dahl & Licht 2016). Kurt *et al.* (2019) showed that pitching foils swimming freely in the cross-stream direction do indeed settle into a stable near-ground equilibrium altitude under no control. By showing good agreement between the equilibrium altitudes calculated through inviscid potential flow simulations and those measured in viscous water channel experiments, they determined that stable equilibrium altitudes are an inviscid phenomenon (Kurt *et al.* 2019). Zhong *et al.* (2019) broadened our understanding of these equilibrium altitudes by studying hydrofoils of varying aspect ratio. They discovered that near-ground equilibrium altitudes can be stable, unstable or absent, depending upon the aspect ratio and Strouhal number.

The equilibrium altitude can determine the relative spacing between the swimmer and the boundary, which can significantly affect the hydrodynamics and propulsive performance of near-ground swimmers. To better design and control the equilibrium altitude, now, it is essential to understand the underlying physics that give rise to equilibrium altitudes. In this study, we uncover the fundamental forces that balance to generate equilibrium altitudes. Following the classic force decomposition of von Kármán & Sears (1938) and Mccune & Tavares (1993), we advance our understanding in two important ways: (i) we reveal the mechanism behind equilibrium altitudes and (ii) we leverage this understanding to develop scaling laws to predict equilibrium altitudes from only the input kinematics. Previously, Kurt *et al.* (2019) proposed that stable equilibrium altitudes are generated by a balance of the added mass lift, wake-induced lift and quasi-steady lift. However, their force decomposition approach implicitly assumed that the local effective flow velocity acting on a foil was unaltered due to the presence of the ground. In this study, we no longer make this assumption and, in fact, we determine that this effect is integral to our understanding of the mechanism behind equilibrium altitudes. We will show that, upon deeper investigation, equilibrium altitudes exist due to a balance between the positive wake-induced lift and negative quasi-steady lift, with added mass lift playing precisely zero role – effectively a scallop theorem result (Purcell 1977) for the time-averaged lift. In this way, our new understanding of the stable equilibrium altitude mechanism supersedes that which was proposed in Kurt *et al.* (2019).

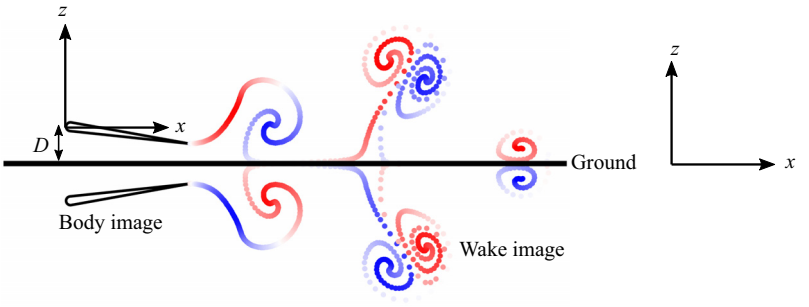

Figure 1. Illustration of a hydrofoil pitching near the ground. An inertial frame of reference fixed to the undisturbed fluid is denoted by (X, Z) while a body-fixed frame of reference is denoted by (x, z). An image system enforces a no-flux boundary condition at the ground plane ($Z = 0$).

2. Methods

2.1. *Problem formulation*

In this study, a simple model of a pitching hydrofoil is used to represent a swimmer propelling itself in an unsteady ground effect (figure 1). The foil is a 7 % thick teardrop-shaped cross-section (Godoy-Diana, Aider & Wesfreid 2008; Quinn *et al.* 2014*b*; Kurt *et al.* 2019) with a chord length of $c = 0.095$ m. The foil undergoes sinusoidal pitching about its leading edge

$$\theta(t) = \theta_0 \sin(2\pi f t), \tag{2.1}$$

where $\theta(t)$ is the instantaneous pitching angle, θ_0 is the pitching amplitude, f is the pitching frequency and t is time. The pitching angle is considered positive for clockwise pitching rotations about the leading edge. The trailing-edge peak-to-peak amplitude A is defined by

$$A = 2c \sin\theta_0, \tag{2.2}$$

and its dimensionless counterpart is $A^* = A/c$. The reduced frequency and the Strouhal number are defined as

$$k = \frac{fc}{U_\infty}, \quad St = \frac{fA}{U_\infty}, \tag{2.3a,b}$$

where U_∞ is the swimming speed of the foil. The ground proximity, D, is considered as the distance from the foil's leading edge to the ground plane (figure 1) and its dimensionless form is $D^* = D/c$. Finally, the lift force L is normalized by the dynamic pressure to give lift coefficient,

$$C_L = \frac{L}{1/2\rho c s U_\infty^2}, \tag{2.4}$$

where ρ is the fluid density while the span length s is set to unity for two-dimensional simulations, and $s = \mathit{AR}c$ for three-dimensional simulations, with AR being the aspect ratio. Its time-averaged form is given as

$$\bar{C}_L = \frac{\bar{L}}{1/2\rho c s U_\infty^2}, \tag{2.5}$$

where $\bar{L}$ is the time-averaged lift.

2.2. *Numerical methods*

The simulations model a potential flow that is assumed to be irrotational, incompressible and inviscid. This flow is governed by Laplace's equation, $\nabla^2\Phi^* = 0$, where Φ^* is the perturbation velocity potential in an inertial frame fixed to the undisturbed fluid. A no-flux boundary condition, $\nabla\Phi^* \cdot \boldsymbol{n} = 0$, where $\boldsymbol{n}$ is the surface normal vector, must be satisfied on the body surface and the ground plane at $Z = 0$, and a far-field boundary condition such that flow perturbations decay far away from the body and its wake surfaces must be satisfied.

Following previous studies (Katz 1985; Quinn *et al.* 2014*b*; Moored 2018; Kurt *et al.* 2019; Zhong *et al.* 2019; Mivehchi *et al.* 2021), this potential flow problem is solved numerically using an unsteady boundary element method with the method of images used to enforce the ground plane boundary condition. In this method, the foil, its wake surfaces and their images are discretized into a finite number of boundary elements. The general solution to the potential flow problem is then reduced to finding a distribution of constant-strength doublet and source elements that satisfy the body and ground plane boundary conditions. The boundary elements also implicitly satisfy the far-field boundary condition. The body boundary condition is imposed using a Dirichlet condition at collocation points centred on each body element, but pushed within the body along the element's surface normal. Also, an explicit Kutta condition is applied where the vorticity at the trailing edge is zero by tuning the strength of a wake boundary element at the trailing edge. At each time step, the trailing-edge element is shed with a strength that satisfies Kelvin's circulation theorem and it remains constant thereafter. A wake roll-up algorithm is implemented to advect the wake elements with the local velocity calculated by the desingularized Biot–Savart law (Krasny 1986; Zhu *et al.* 2002; Moored 2018; Akoz, Mivehchi & Moored 2021). Therefore, a matrix representation of the boundary condition is formed and solved for the body doublet strengths at each time step. The perturbation velocity over the surface of the body is then determined by a local differentiation of the perturbation potential.

Following the work of Moored (2018), the pressure exerted on the body is calculated by the unsteady Bernoulli equation as

$$P(x, z, t) = -\rho\frac{\partial\Phi^*}{\partial t} + \rho(\boldsymbol{u_{rel}} + \boldsymbol{U}_\infty) \cdot \nabla\Phi^* - \rho\frac{(\nabla\Phi^*)^2}{2}, \tag{2.6}$$

where $\boldsymbol{u_{rel}}$ is the local surface velocity of the pitching foil relative to the body-fixed frame of reference. The inviscid instantaneous resultant force is then simply an integration of the instantaneous pressure field acting over the body surface. Finally, the resultant force is decomposed into its lift and drag directions. For more details see Moored (2018).

2.3. *Force decomposition approach*

Following the classic force decomposition of von Kármán & Sears (1938) and Mccune & Tavares (1993), the lift force can be decomposed as the sum of the added mass lift, quasi-steady lift and wake-induced lift, which are denoted by $(\cdot)_a$, $(\cdot)_q$ and $(\cdot)_w$, respectively. We apply this decomposition approach directly to the pressure field defined by the unsteady Bernoulli equation.

To calculate the added mass pressure, P_a, potential flow simulations are employed where there are no wake elements shed and no Kutta condition enforced. Under these conditions, the first term in (2.6) is known as the added mass pressure. To calculate the quasi-steady pressure, P_q, potential flow simulations are employed where there are no wake elements

shed, but there is a Kutta condition enforced (modelled in the boundary element method with a trailing-edge panel that extends far from the foil, effectively to infinity). Then the combined second and third terms in (2.6) provide the quasi-steady pressure. The combined added mass and quasi-steady pressures are

$$P_a(x,z,t)+P_q(x,z,t)=\left[\underbrace{-\rho\frac{\partial\Phi^*}{\partial t}}_{\textit{added mass}}+\underbrace{\rho(\boldsymbol{u_{rel}}+\boldsymbol{U}_\infty)\cdot\nabla\Phi^*-\rho\frac{(\nabla\Phi^*)^2}{2}}_{\textit{quasi-steady}}\right]_{NO\ WAKE}. \tag{2.7}$$

The wake-induced pressure, P_w, is calculated as the difference between the total pressure, P (calculated from the full simulations described in § 2 by (2.6)), and the combined added mass and quasi-steady pressures

$$P_w(x,z,t)=P(x,z,t)-\left[P_a(x,z,t)+P_q(x,z,t)\right]. \tag{2.8}$$

Finally, each force component is acquired by integrating its corresponding pressure field over the body. Then the added mass, quasi-steady and wake-induced lift coefficients can be defined and they sum to the total lift coefficient

$$C_L=C_{L_a}+C_{L_q}+C_{L_w}. \tag{2.9}$$

2.4. *Force decomposition validation*

Before applying the force decomposition approach to simulations of a pitching foil in ground effect, we first validated it against Theodorsen's solution, which provides a test case where the added mass, quasi-steady and wake-induced terms are readily identified (Bisplinghoff, Ashley & Halfman 2013). In Theodorsen (1935), the lift force generated by a foil pitching about its leading edge is

$$L=\underbrace{\rho\pi\frac{c^2}{4}\left(U_\infty\dot\theta+\frac{c}{2}\ddot\theta\right)}_{\textit{added mass}}+\underbrace{\rho\pi U_\infty c\left(U_\infty\theta+\frac{3c}{4}\dot\theta\right)}_{\textit{quasi-steady}}$$
$$+\underbrace{[C(k)-1]\,\rho\pi U_\infty c\left(U_\infty\theta+\frac{3c}{4}\dot\theta\right)}_{\textit{wake-induced}}, \tag{2.10}$$

where $C(k)$ is the lift deficiency function. Full boundary element simulations and their decomposition counterparts were performed as described in §§ 2.2 and 2.3 on a thin airfoil (1 % thick teardrop shape), undergoing small pitching amplitudes of motion about its leading edge ($A^*=0.002$), with a frozen wake (no wake roll-up algorithm applied), and across a wide reduced frequency range of $k=0.1$, 1 and 10. Figure 2 shows that all three lift components precisely match the Theodorsen solution across a wide range of k. Even though Theodorsen's solution makes several assumptions, it is worth noting that the force decomposition approach itself is generic and has no underlying assumptions.

2.5. *Experimental methods*

We conducted four groups of experiments to facilitate the force decomposition analysis, including a two-dimensional (2-D) static ground effect test, a 2-D unsteady high-frequency

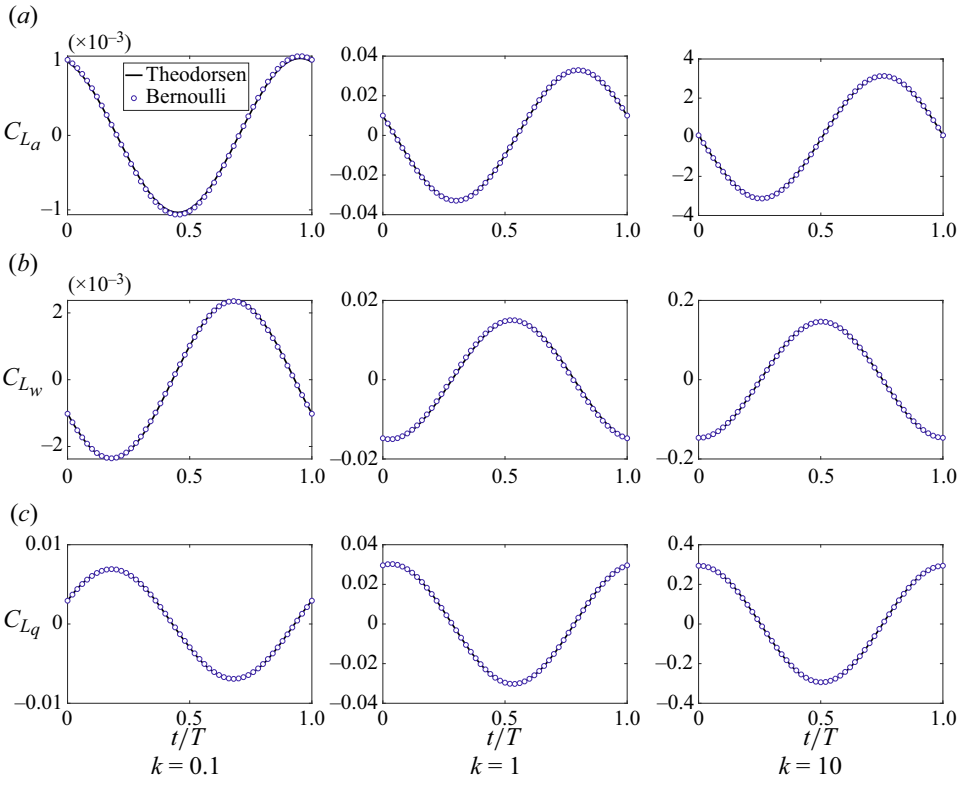

Figure 2. Validation of the force decomposition approach against Theodorsen's solution across a wide reduced frequency range of $0.1 \leq k \leq 10$. The panel rows show: (*a*) added mass lift, (*b*) wake-induced lift and (*c*) quasi-steady lift.

test (for wake deflection analysis) and a 2-D and a 3-D unsteady ground effect test. All hydrofoils had a teardrop cross-section with a chord length of 0.095 m to ensure consistency with simulations, and were 3D-printed with solid ABS (Acrylonitrile Butadiene Styrene). A stainless steel driveshaft with a diameter of 6.35 mm was used to pitch the hydrofoil at its leading edge, with the pitch angle θ being prescribed as $\theta_0 \sin(2\pi ft)$. The driveshaft was driven by a high-torque digital servo motor (Dynamixel MX64), while an absolute encoder (US Digital A2K 4096 CPR) was utilized to verify the angle of the actual motion. The forces and moments generated were measured using a six-axis force-torque sensor (ATI-Mini 40: SI-40-2). The lateral forces were time averaged over 30 seconds or 20 oscillation cycles to determine the mean lift force for static and unsteady tests. The incoming flow speed was set to $143\,\mathrm{mm\,s^{-1}}$ using an ultrasonic flowmeter (Dynasonics Series TFXB), resulting in a chord-based Reynolds number of 13 500. For ground effect tests, an additional splitter plate was used instead of a tunnel sidewall to control the boundary layer thickness (figure 3). A boundary layer thickness of $\delta_{99\,\%} \approx 7.5$ mm ($\delta_{99\,\%}/c = 0.08$) was measured using particle image velocimetry at the position aligned with the leading edge of the hydrofoil.

For all 2-D tests, we used a hydrofoil of aspect ratio 3 in a nominally 2-D flow condition, which was achieved by installing a horizontal splitter plate and a surface plate near the tips of the hydrofoil. The gap between the hydrofoil tips and the surface/splitter plate was less than 5 mm and surface waves were also minimized by the presence of the surface plate.

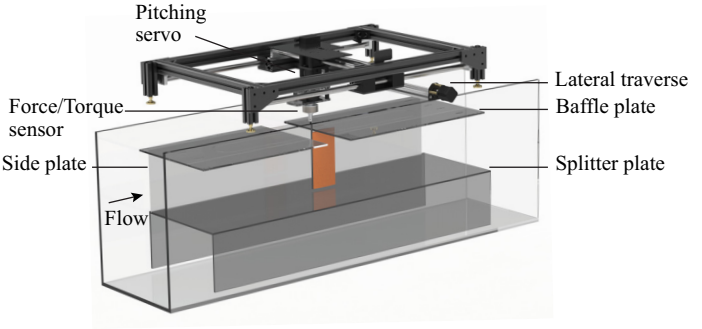

Figure 3. Schematic of experiment set-up equipped with removable splitter plate.

	Varying k	Varying St
k	0.55–1	1
St	0.3	0.25–0.55
D^*	0.25–1.5	0.25–1.5

Table 1. Simulation variables investigated in the current study.

To validate the 3-D force decomposition, we repurposed the 3-D unsteady ground effect data that were previously published in Zhong *et al.* (2019). We tested hydrofoils with four aspect ratios: 1, 1.5, 2 and 2.5, and assessed their performance over a range of ground proximities. Each trial was repeated three times.

3. Force decomposition results

A pitching foil in ground effect and constrained to fixed ground distances was simulated across a wide range of dimensionless ground proximities, reduced frequencies and Strouhal numbers, and force decomposition was applied as described in § 2.3. The simulation variables are detailed in table 1.

3.1. *Mechanism behind the generation of stable and unstable equilibria*

The pitching foil examined in this study is effectively out of ground effect by $D^* = 1.5$ for cases with $St < 0.45$, and by $D^* = 2$ for cases with higher St. In fact, a typical reverse von Kármán vortex street, indicative of thrust production in an infinite domain, is observed when $D^* = 1.5$, $k = 1$ and $St = 0.3$ (figure 4*a*). As the foil approaches the ground to a distance of $D^* = 0.4$ ($k = 1$ and $St = 0.3$), the wake vortices deflect away from the ground (figure 4*b*), an effect that has been attributed to the image vortex system (Quinn *et al.* 2014*b*).

The total lift for all of the simulations is presented for varying reduced frequency and ground distance ($St = 0.3$; figure 4*c*), and for varying Strouhal number and ground distance ($k = 1$; figure 4*d*,*e*). A common trend emerges in all of the in-ground effect data except when $St > 0.475$: the lift is positive close to the ground (pushing a foil away from the ground) and negative far from the ground (pulling a foil towards the ground), crossing zero (stable equilibrium altitude; solid lines in figure 4) between these two regimes. As observed previously, the stable equilibrium altitude increases with increasing

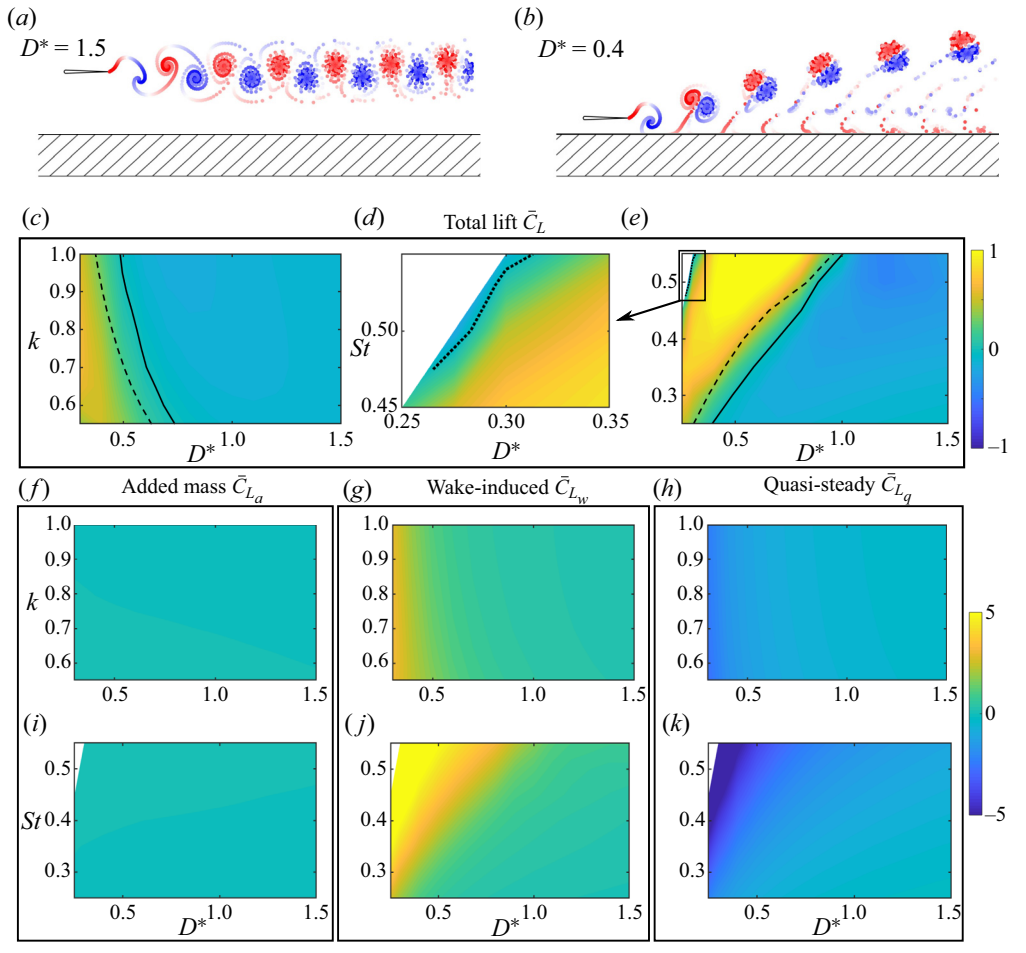

Figure 4. Both the stable and unstable equilibrium altitudes are generated by a balance between the positive wake-induced lift and negative quasi-steady lift. (*a*) Wake plots for an out-of-ground effect foil. (*b*) Wake plots for a near-ground foil. (*c*) Total lift for varying k with $St = 0.3$. (*e*) Total lift for varying St with $k = 1$. (*d*) Zoom-in plot highlighting the unstable equilibrium altitude. (*f*,*i*) Added mass lift. (*g*,*j*) Wake-induced lift. (*h*,*k*) Quasi-steady lift. Note that the stable equilibrium altitude is marked by a solid line, the stable equilibrium altitude for a foil unconstrained in the cross-stream direction (mass of the foil is chosen to be $m = 2.68\rho sc^2$) is marked by the dashed line and the unstable equilibrium altitude is marked by the dotted line.

St and decreasing k (Kurt *et al.* 2019), and an unstable equilibrium altitude emerges when $St > 0.475$ (dotted line in figure 4*d*), which increases slightly with increasing St in a narrow near-ground region (Zhong *et al.* 2019). Altitudes below/above the unstable equilibria produce a negative/positive lift, demonstrating that it is indeed unstable. For the first time, this unstable equilibrium altitude is observed in simulation, which corroborates previous experimental findings (Zhong *et al.* 2019).

The dashed lines in figures 4(*c*) and 4(*e*) show the unconstrained simulation results from Kurt *et al.* (2019). As discovered in Cochran-Carney (2018), the observed difference in the equilibrium altitudes of the constrained and unconstrained cases is ultimately caused by a difference in the unconstrained simulation's dimensionless mass ($m^* \equiv m/(\rho sc^2) = 2.68$) compared with that of the constrained simulations ($m^* = \infty$). The finite mass foils of the unconstrained simulations have a finite heaving recoil while the effectively infinite

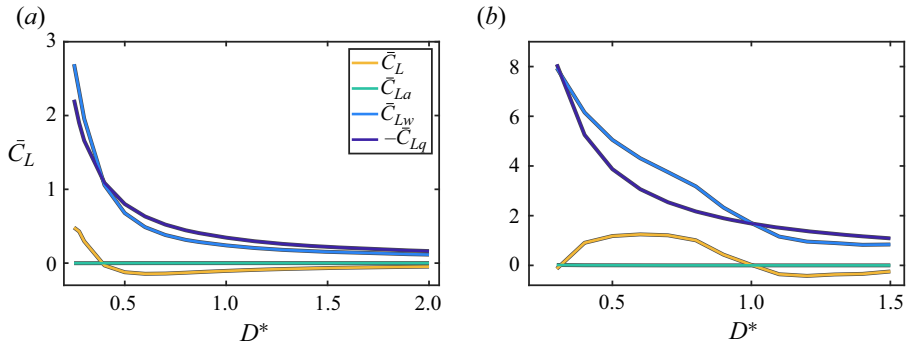

Figure 5. Force decomposition for $k = 1$: (*a*) $St = 0.25$ and (*b*) $St = 0.55$.

mass foils of the constrained simulations have zero heaving recoil, thereby altering the force production between the two cases and, consequently, their equilibrium altitudes. Despite these differences, the constrained equilibria show all of the same trends as the unconstrained equilibria with only a small shift in their D^* location. Moreover, this study will focus on constrained simulations by design since these allow us to investigate the forces outside of equilibrium conditions, which is essential to fully understand the stability properties of the equilibria.

The decomposition of the lift coefficient into its added mass, wake-induced and quasi-steady components (figure 4*f–k*) shows clear trends in the components for all ground proximities and kinematics. The added mass lift is always precisely zero and therefore does not play a role in generating equilibrium altitudes (figure 4*f*,*i*). For in-ground effect data, the wake-induced lift is always positive (figure 4*g*,*j*) while the quasi-steady lift is always negative (figure 4*h*,*k*), revealing that both unstable and stable equilibria are generated by a balance between positive wake-induced lift and negative quasi-steady lift. The magnitudes of the wake-induced and quasi-steady lift increase with increasing St and decreasing k.

The data contours in figure 4 reveal the basic mechanism behind the existence of equilibria, but they do not provide a clear picture as to why there can be both a stable and an unstable equilibria for a given St and k. To better understand this feature of the data, the lowest and highest St cases with $k = 1$, $St = 0.25$ and $St = 0.55$, respectively, are presented in figure 5. For low St (figure 5*a*), the total lift only crosses zero at one D^*, producing a stable equilibrium. This equilibrium altitude is stable since, for altitudes above equilibrium, the magnitude of the quasi-steady lift is greater than the wake-induced lift, leading to a net negative total lift force, and for altitudes below equilibrium the magnitude of the wake-induced lift is greater than the quasi-steady lift, leading to net positive total lift. For high St (figure 5*b*), the total lift is seen to cross through two equilibrium altitudes. Now, it becomes clear that the wake-induced lift magnitude curve crosses through the quasi-steady lift magnitude curve at two ground distances because the wake-induced lift has a nearly linear increase with decreasing ground distance while the quasi-steady lift has an exponential growth for $D^* < 1.1$. In fact, the slopes of the lift components at the equilibrium points determine their stability: when $|\mathrm{d}\bar{C}_{Lq}/\mathrm{d}D^*| < |\mathrm{d}\bar{C}_{Lw}/\mathrm{d}D^*|$ the equilibrium altitude is stable and when $|\mathrm{d}\bar{C}_{Lq}/\mathrm{d}D^*| > |\mathrm{d}\bar{C}_{Lw}/\mathrm{d}D^*|$ the equilibrium altitude is unstable.

Although this analysis has revealed the basic mechanism behind the generation of stable and unstable equilibrium altitudes, it also raises several questions. How does added mass lift integrate precisely to zero when we expect peak negative added mass lift to be larger in

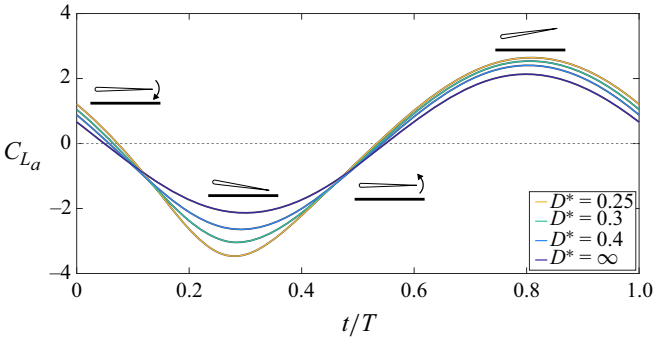

Figure 6. The added mass lift as a function of time for varying ground distance with $k = 1$ and $St = 0.3$. Out-of-ground effect data are represented by $D^* = \infty$.

magnitude than the peak positive added mass lift since the foil will get closer and further from the ground throughout an oscillation cycle? Why is the wake-induced lift positive for a wake deflected away from a ground plane when, based on momentum flux arguments, we would expect the opposite? Why is the quasi-steady lift negative in nature? To address these questions, the following sections will examine each force component more deeply.

3.2. *Added mass lift*

As shown in the previous section, the time-averaged added mass lift is precisely zero for all of the simulation cases. This is expected for solutions to the linear potential flow equations with harmonic boundary conditions – a 'scallop theorem' result (Purcell 1977). However, for the in-ground effect data it is well-known that, as the ground distance decreases, there is an increase in the added mass of a foil (Brennen 1982; Mivehchi *et al.* 2021). This effect should amplify both the positive and negative peaks in the added mass lift, but should more greatly amplify the negative peak, which occurs at the bottom of the down stroke when the foil is closest to the ground. Considering only these peak forces, one would imagine that the time-averaged added mass lift would be negative, yet we know that it is zero from the data in § 3.1, so how does the added mass lift integrate precisely to zero and satisfy a scallop theorem?

Figure 6 presents the time-varying added mass lift at four ground distances when $k = 1$ and $St = 0.3$. Indeed, as the ground distance decreases, both the positive and negative peaks grow in magnitude, and it is true that the negative peak is amplified more than the positive peak, creating a net negative lift in the peak forces. However, it is now clear that the negative peak becomes sharper while the positive peak becomes broader. When integrating the lift over a full cycle, this effect counteracts the net imbalance in the positive and negative peak forces, leading to a precisely zero time-averaged force.

Although our simulations were for potential flow, the phenomenon of the time-averaged added mass lift being precisely zero is also valid in viscous flow. According to Graham, Pitt Ford & Babinsky (2017), in viscous flow, the added mass lift of a foil is the time derivative of the quasi-steady vortex impulse in the cross-stream direction, which is

$$L_a = -\rho \frac{\mathrm{d}I_z}{\mathrm{d}t}, \quad \text{and} \quad I_z = -\int x\gamma_0 \,\mathrm{d}S, \tag{3.1a,b}$$

where x is the coordinate of the body-fixed frame of reference, γ_0 is the bound quasi-steady vortex sheet, S is the body surface and I_z is the vortex impulse. These equations suggest

that, since the quasi-steady bound circulation is a periodic signal for a foil periodically pitching near the ground, then the vortex impulse is also a periodic signal. When the added mass lift is then time averaged over a period of motion, it is necessarily zero since it is the time derivative of the vortex impulse.

3.3. *Wake-induced lift*

In § 3.1, the wake-induced lift was found to be positive for in-ground effect foils regardless of their ground distance and kinematics. This is surprising, since the wake vortices deflect away from the ground and in the time average they also produce a momentum jet deflected away from the ground (Quinn *et al.* 2014*b*). If one imagines a control volume around a foil and considers only the momentum flux term, the deflection of the jet away from the ground should have an associated negative lift force, that is, a force pushing the swimmer toward the ground (Kurt *et al.* 2019), and yet the data from § 3.1 show otherwise.

To understand this phenomenon more deeply we employ a control volume analysis. To begin, we will consider a simple out-of-ground effect case where a deflected wake is also generated very much akin to the deflected wake of in-ground effect foils. This case is useful since it will help unambiguously show the connection among the wake-induced lift, the pressure field and the momentum flux, and it presents an opportunity to experimentally verify the trends in the wake-induced lift. With this basic knowledge in mind, we will then proceed to the in-ground effect case.

When a 2-D pitching foil oscillates at sufficiently high Strouhal number, it is well documented (Marais *et al.* 2012; Das, Shukla & Govardhan 2016) that there is a wake instability that causes the wake vortices to form vortex dipoles and, in turn, deflect the wake. Figure 7(*a*) shows an example of this, where a pitching foil is operated at $St = 0.55$ and $A^* = 0.3$. Since this pitching foil is out of ground effect and has a symmetric motion, then the time-averaged added mass and quasi-steady lift must both necessarily be zero. However, due to the wake deflection the time-averaged wake-induced lift will be non-zero and, in fact, it will be the only component thus making it equivalent to the total lift in this specific case.

Following the work of Cleaver, Wang & Gursul (2012), a time-averaged control volume analysis can be applied to the control volume (dashed box) defined in figure 7(*a*)

$$\bar{L}_w = \overline{\underbrace{\int_{UL} \Delta P_{UL}\,\mathrm{d}A}_{\textit{Pressure difference}}} \; \overline{\underbrace{-\int_{CS} \rho v(\boldsymbol{V}\cdot\boldsymbol{n})\,\mathrm{d}A}_{\textit{Momentum flux}}}, \tag{3.2}$$

where the total time-averaged lift is precisely equal to the time-averaged wake-induced lift, $\bar{L}_w$, the pressure difference between the upper and lower (UL) control surfaces is ΔP_{UL}, the velocity field is $\boldsymbol{V}$, the vector normal to the control surfaces (CS) is $\boldsymbol{n}$ and the horizontal and vertical components of the velocity field are u and v, respectively. In this sense, the wake-induced lift consists of a momentum flux term and a pressure difference term. The left bottom corner of the control volume is c from the foil's leading edge vertically and $0.25c$ horizontally. The vertical and horizontal dimensions of the volume, C_z and C_x, are fixed at $2c$ and $4c$, respectively.

Just like the in-ground effect data from § 3.1, both simulations and experiments show that the wake-induced lift is in fact positive for an upward deflected wake (figure 7*c*) which, in the case of this out-of-ground effect foil, is consistent with previous findings (Emblemsvåg, Suzukiy & Candlerz 2002; Liang *et al.* 2011; Cleaver *et al.* 2012; Yu, Hu & Wang 2012). Using the simulation data, figure 7(*c*) further shows that the wake-induced lift

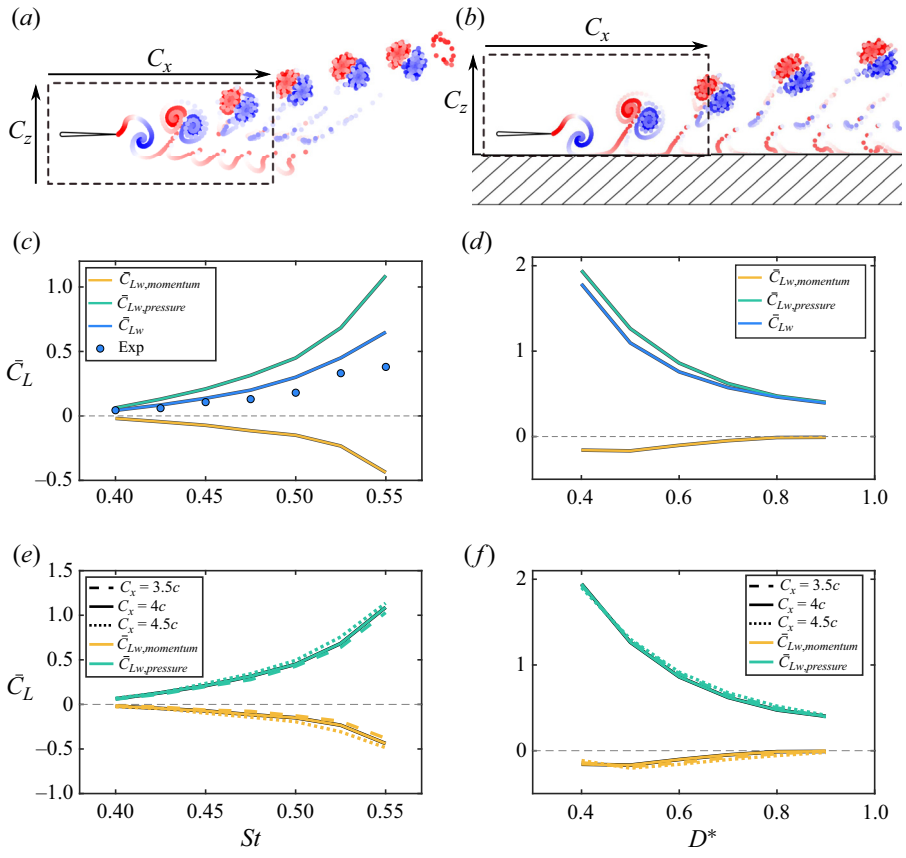

Figure 7. Time-averaged lift control volume analysis. The control volume is represented by a dashed box, where C_z and C_x are the vertical and horizontal dimensions of the volume, respectively. Here, C_z is fixed at $2c$ and C_x is fixed at $4c$ in (c,d), but varied in (e,f). (a) Upward deflected wake generated by an out-of-ground effect foil pitching at $St = 0.55$ and $A^* = 0.3$. (b) Upward deflected wake generated by an in-ground effect foil pitching at $St = 0.3$ and $A^* = 0.3$. (c) Control volume analysis for the out-of-ground effect case. (d) Control volume analysis for the in-ground effect case. (e) Size effect of the control volume for the in-ground effect case. (f) Size effect of the control volume for the out-of-ground effect case. The time-averaged wake-induced lift coefficient from simulations and experiments are denoted by the blue lines and blue circles, respectively. Contributions to simulations' wake-induced lift from the pressure difference term and the momentum flux term in the control volume analysis are shown as green and yellow lines, respectively.

from the net momentum flux term is indeed negative, as expected, while the contribution from the pressure difference term is positive and, surprisingly, is larger in magnitude than the momentum flux term, thereby making the wake-induced lift positive for an upward deflected wake. In light of this analysis, momentum flux considerations alone do not accurately discern the direction of forces generated by an asymmetric wake; the pressure field must also be considered.

Moreover, the same control volume analysis was applied to an in-ground effect pitching foil in figure 7(b), which was calculated by (3.3) and (3.4). The left bottom corner of the control volume is D from the foil's leading edge vertically and $0.25c$ horizontally. The vertical and horizontal dimensions of the volume, C_z and C_x, are fixed at $2c$ and $4c$, respectively. Since the time-averaged added mass lift is zero (§ 3.2), the time-averaged wake-induced lift from the pressure difference and momentum flux terms are acquired by

calculating those two contributions for the total and quasi-steady pressure and flow fields and taking their differences as

$$\bar{L}_{w,pressure} = \overline{\int_{UL} \Delta P_{UL}\,\mathrm{d}A}\Big|_{total} - \overline{\int_{UL} \Delta P_{UL}\,\mathrm{d}A}\Big|_{quasi\text{-}steady}, \tag{3.3}$$

and

$$\bar{L}_{w,momentum} = -\overline{\int_{CS} \rho v(\boldsymbol{V}\cdot\boldsymbol{n})\,\mathrm{d}A}\Big|_{total} + \overline{\int_{CS} \rho v(\boldsymbol{V}\cdot\boldsymbol{n}),\mathrm{d}A}\Big|_{quasi\text{-}steady}. \tag{3.4}$$

Figure 7(*d*) shows that, in ground effect, the momentum flux term is negative, yet the wake-induced lift acts in the positive direction since the pressure difference term again outweighs the momentum flux term, as in the out-of-ground effect case. It is worth noting that compared with the out-of-ground effect case the pressure difference term now has a more significant effect on the wake-induced lift.

To show that the conclusion of the pressure difference term determining the direction of the wake-induced lift is not affected by the size of the control volume, C_x of the control volume is varied from $3.5c$ to $4.5c$ for both out-of-ground and in-ground cases numerically (figure 7*e*,*f*). It is discovered that the magnitudes of the two terms stay nearly constant, and still, the magnitude of the positive pressure difference term is larger than that of the negative momentum flux term. Our simulations and the experiments in Cleaver *et al.* (2012) suggest that, as long as the momentum flux crosses the control volume boundary, the conclusion that the pressure difference term determines the direction of the wake-induced lift still holds.

3.4. *Quasi-steady lift*

To provide deeper insight as to why there is a net negative quasi-steady force in the time average, we further break down the quasi-steady lift into its constituent components by leveraging the Kutta–Joukowski theorem (von Kármán & Sears 1938), $L_q = \rho s U \Gamma_0$, where L_q is the quasi-steady lift, s is the span length, U is the local effective flow velocity acting on a foil and Γ_0 is the quasi-steady bound circulation of a foil. The local effective velocity is calculated from simulations by summing the free-stream velocity, U_∞, with the induced velocity U_i at the leading edge from the image body. The quasi-steady bound circulation is simply the negative of the strength of the trailing-edge panel used to enforce the Kutta condition in the boundary element simulations, that is, $\Gamma_0 = -\mu_{TE}$ (Katz & Plotkin 2005). The Kutta–Joukowski theorem can be non-dimensionalized and written as

$$C_{L_q} = 2U^*\Gamma_0^*, \quad U^* = \frac{U}{U_\infty}, \quad \Gamma_0^* = \frac{\Gamma_0}{cU_\infty}. \tag{3.5a–c}$$

When a foil is out of ground effect then $U^* = 1$, $\Gamma_0^* = \Gamma_{0,\infty}^*$ and $C_{L_q} = C_{L_{q,\infty}}$, where $\Gamma_{0,\infty}^*$ and $C_{L_{q,\infty}}$ are the time-varying quasi-steady bound circulation and lift coefficient for a foil in an infinite domain. The quasi-steady bound circulation has been found to be amplified as the foil gets closer to the ground (Zong, Liang & Zhou 2012; Baddoo *et al.* 2020). This effect comes from the fact that, as the foil approaches the ground, the bound vortex of its image foil induces a transverse velocity at the trailing edge of the real foil. In order for the Kutta condition to be preserved, an additional bound circulation of the real foil must arise to cancel the additional transverse velocity induced by the image foil.

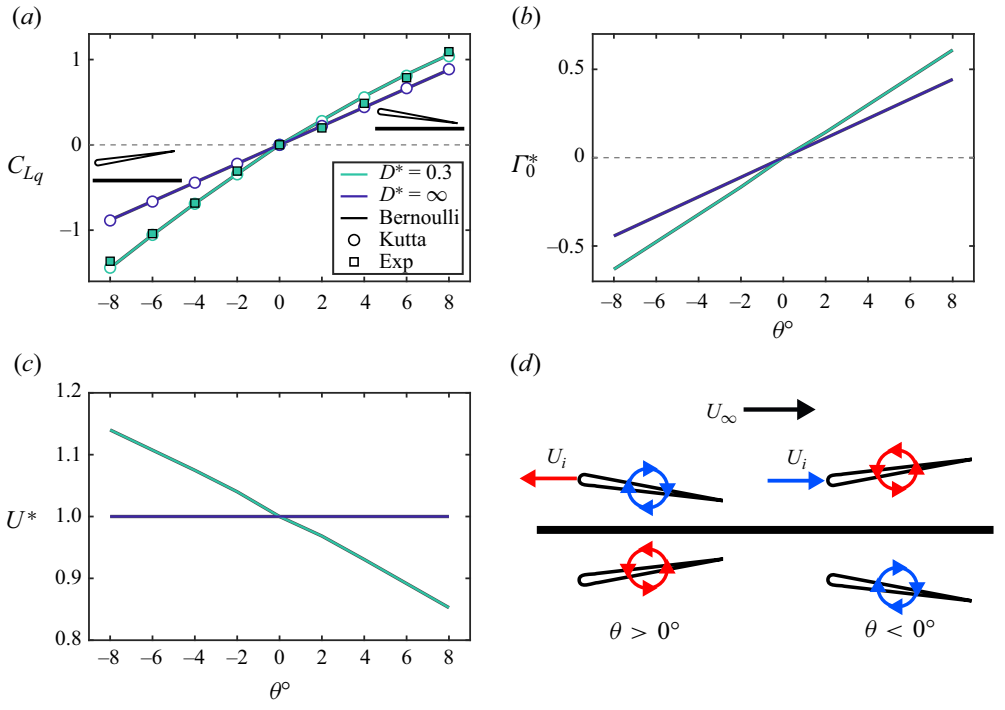

Figure 8. Asymmetry in the quasi-steady lift for a steady foil in ground effect is caused by the velocity induced on a foil by its image body's quasi-steady bound circulation. (*a*) The quasi-steady lift coefficient. Note that the lift coefficient calculated in the simulations (using the unsteady Bernoulli equation) is represented with solid lines, the lift coefficient calculated from the simulations using the Kutta–Joukowski theorem is represented by the circle markers and the experimental data are represented by the square markers. (*b*) The dimensionless quasi-steady circulation. (*c*) The dimensionless effective flow velocity. (*d*) Schematic of the components of the effective flow velocity, U, that is the summation of U_i and U_∞.

Without loss of generality, the quasi-steady bound circulation for in-ground effect foils can then be modelled as the multiplication of a circulation amplification factor β and the infinite domain quasi-steady circulation, $\Gamma_0^* = \beta\Gamma_{0,\infty}^*$. We expect that both the circulation and the effective flow velocity will be amplified or reduced for foils in ground effect as opposed to out-of-ground effect foils.

To understand the connections among the circulation amplification factor, the amplified/reduced effective flow velocity and the quasi-steady lift, as well as to verify these connections with experimental data, we begin with a simple case of a static foil in and out of ground effect at various pitch angles (figure 8). For the static foil, the quasi-steady lift is precisely the total lift, which is readily measured in experiments. Figure 8(*a*) presents the quasi-steady lift for $D^* = 0.3$ and $D^* = \infty$ from the simulations (solid lines), which is directly determined by integrating the pressure acting on the foil calculated from the unsteady Bernoulli equation (§ 2.2). The simulations are also used to calculate the quasi-steady lift by using the Kutta–Joukowski theorem (circle markers) as outlined above, and both approaches are observed to produce exactly the same result. Also, the in-ground effect quasi-steady lift is verified by having good agreement with experimental data (square markers).

For the out-of-ground effect foil, the quasi-steady lift shows the classic linear relationship with the pitch angle for $-8° \leq \theta \leq 8°$. However, when in ground effect

the quasi-steady lift shows a nonlinear relationship with the pitch angle, where both the negative and positive lift regimes are amplified compared with the out-of-ground effect case, yet the negative lift regime is amplified more than the positive lift regime. This produces an asymmetric lift response about $\theta = 0$. If one were to pitch the foil through an 8° amplitude sinusoidal pitching motion at an infinitesimal Strouhal number, this asymmetric lift response would lead to a net negative quasi-steady lift in the time average ($\bar{C}_{L_q} = -0.07$ for simulations and $\bar{C}_{L_q} = -0.09$ for experiments), just as is observed in the quasi-steady data of finite Strouhal numbers. In fact, throughout this section, we will show that precisely the same mechanism is at play in this static case as is in the quasi-steady cases of finite Strouhal number.

Figure 8(*b*) presents the dimensionless quasi-steady circulation. The circulation amplification is observed to be symmetric about $\theta = 0$ and appears to just be a constant factor giving rise to a slope change in the $\Gamma_0^* - \theta$ line. This shows, at least for the static case, that β is only a function of D^*, not θ. Moreover, the circulation amplification is responsible for amplifying the quasi-steady lift forces in ground effect, but is not responsible for asymmetry in the lift curve. Figure 8(*c*) shows that the effective flow velocity increases above the free-stream speed when the quasi-steady circulation is negative (counterclockwise), while it decreases below free-stream speed when the quasi-steady circulation is positive (clockwise). This occurs due to the velocity induced by the quasi-steady bound vortex of the image body (figure 8*d*). By consequence, increased effective flow speed acts to amplify the negative lift of negative pitch angles (negative bound circulation) thereby acting in concert with the circulation amplification effect, and decreased effective flow speed acts to reduce the positive lift of positive pitch angles (positive bound circulation), thereby counteracting the circulation amplification effect. Therefore, it is the change in the effective flow speed that leads to the asymmetric lift response. This mechanism will be implicated further as the reason for the net negative quasi-steady lift for oscillating foils from zero to finite Strouhal numbers.

Figure 9 presents the quasi-steady lift coefficient, dimensionless quasi-steady circulation and dimensionless effective flow velocity for a foil at a range of ground distances with $St = 0.3$. In figure 9(*a*), first, the quasi-steady lift calculated by the unsteady Bernoulli equation and by the Kutta–Joukowski theorem still show good agreement. Figure 9(*b*) shows that the negative and positive quasi-steady circulations are symmetrically amplified with decreasing ground distance, precisely as in the static foil case. Moreover, figure 9(*c*) shows that the effective flow velocity increases above and decreases below the free-stream velocity when the bound circulation is negative and positive, respectively, also mirroring the static foil case. Consequently, the change in effective flow velocity leads to an enhancement in the negative lift and a reduction in the positive lift thereby generating a net negative quasi-steady lift in the time average over one pitching cycle. Figure 9(*d*) illustrates precisely the same effective flow altering mechanism of the image body's quasi-steady circulation as is in the static foil case.

3.5. *Three-dimensional decomposition*

In figure 10(*a*), both 3-D simulations and experiments observe that the stable equilibrium altitude disappears when the aspect ratio decreases to $\mathcal{AR} = 1$, which is reproduced from Zhong *et al.* (2019). Figure 10(*b*), presents the lift decomposition of the 3-D simulations into the added mass, quasi-steady and wake-induced components. Exactly as in the 2-D simulations, a stable equilibrium altitude arises for foils of finite $\mathcal{AR}$ by a balance between the positive wake-induced lift and negative quasi-steady lift. The equilibrium altitude

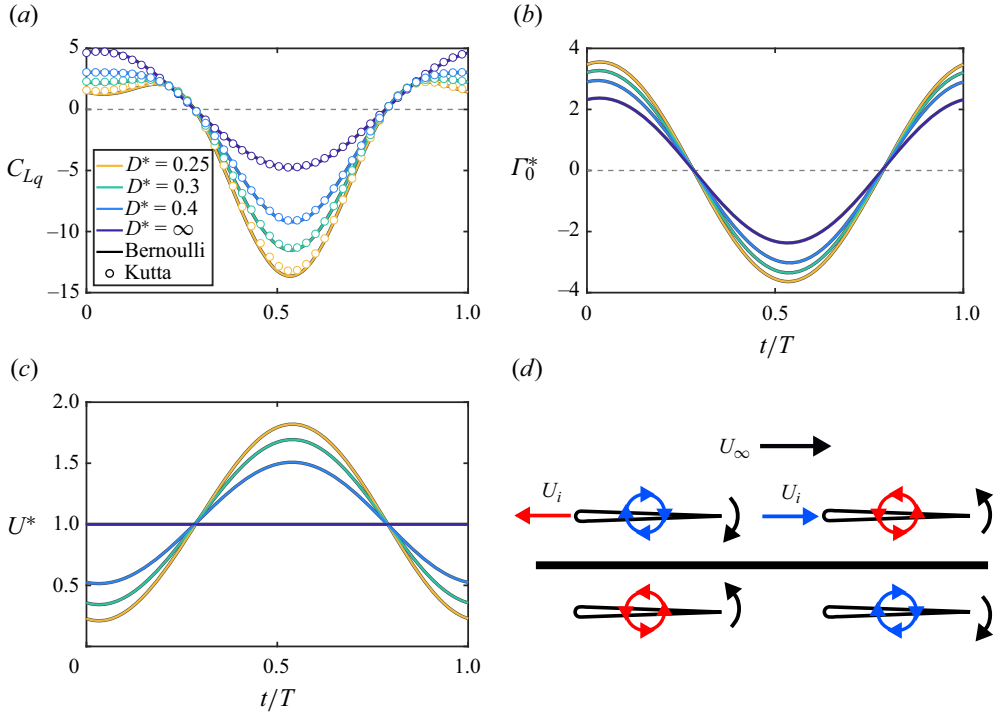

Figure 9. The velocity induced by the ground image body creates asymmetry in the quasi-steady lift at finite Strouhal numbers just like the steady foil case. (*a*) The quasi-steady lift coefficient. (*b*) The dimensionless quasi-steady circulation. (*c*) The dimensionless effective flow velocity. (*d*) Schematic showing the effective flow velocity, U, is the summation of U_i and U_∞.

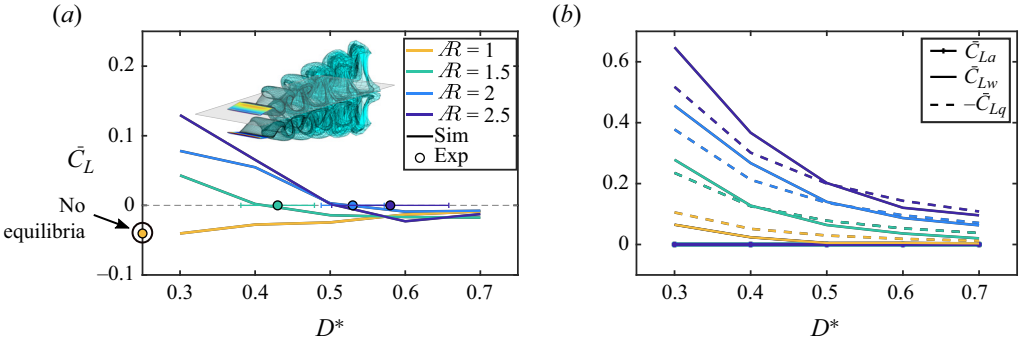

Figure 10. The magnitude of the wake-induced lift of 3-D foils degrades more with decreasing $\mathcal{AR}$ than their quasi-steady lift leading to the disappearance of an equilibrium altitude for $\mathcal{AR} < 1.5$. Simulation data of pitching 3-D hydrofoils of varying aspect ratio with $St = 0.25$ and $\theta_0 = 11^\circ$. (*a*) Total lift as calculated from the simulations. Note that the circle markers represent the stable equilibrium altitudes measured by experiments. (*b*) Decomposed lift components from the simulations.

disappears for low aspect ratio ($\mathcal{AR} < 1.5$) hydrofoils, which instead experience a net negative time-averaged lift force. The decomposition reveals that this occurs since the magnitude of the wake-induced lift reduces more with decreasing $\mathcal{AR}$ than the reduction in the magnitude of quasi-steady lift, thereby having the negative quasi-steady lift outweigh the positive wake-induced lift at all ground distances.

3.6. *Scaling the equilibrium altitude*

The analysis of the added mass, quasi-steady and wake-induced forces presented above can now be leveraged to develop scaling laws that capture the physics of ground effect and are capable of predicting the equilibrium altitude of a pitching foil. Since the added mass forces do not play a role in the generation of an equilibrium altitude then scaling laws for only the quasi-steady and wake-induced lift are sought, two flow models were used to develop the scaling laws for the quasi-steady lift and wake-induced lift, respectively, which enables us to pinpoint any sources of the modelling error in the scaling laws.

3.6.1. *Quasi-steady lift*

As presented in § 3.4, the quasi-steady lift coefficient is

$$C_{L_q} \propto U^* \beta \Gamma^*_{0,\infty}, \tag{3.6}$$

$$\Gamma^*_{0,\infty} = \pi\theta + \frac{3\pi c\dot{\theta}}{4U_\infty}, \tag{3.7}$$

where β is the quasi-steady circulation amplification factor, U^* is the normalized effective flow velocity at the foil's leading edge and $\Gamma^*_{0,\infty}$ is simply the formula for a flat plate pitching about its leading edge from Theodorsen (1935) and Mccune & Tavares (1993). To determine a scaling law for the quasi-steady lift, consider a simplified flow model where the quasi-steady bound vortex is located along the chord (figure 9*d*). Then a scaling relation for the circulation amplification factor and the effective flow velocity can be determined. The circulation amplification factor is calculated by finding the circulation amplification necessary to enforce the Kutta condition at the foil's trailing edge due to the influence of the image quasi-steady bound vortex. Assuming that the distance between the bound vortex and foil's leading edge is bc with $0 \leq b \leq 1$, then the circulation amplification factor is simply calculated as

$$\beta = 1 + \frac{(1-b)^2}{4D^{*2}} \quad \text{where } b = 0.55. \tag{3.8}$$

To determine the placement of the bound vortex along the chord, circulation amplification data at $D^* = 0.5$ from an exact solution for a steady foil in ground effect (figure 4(*d*) in Baddoo *et al.* 2020) were used to determine that $b = 0.55$. The effective flow velocity is calculated by finding the normalized induced velocity at the leading edge, $U^*_i = U_i/U_\infty$, from the image foil's quasi-steady bound vortex

$$U^* = 1 + U^*_i \quad \text{where } U^*_i = \frac{-\Gamma^*_{0,\infty}\beta}{\pi}\left(\frac{D^*}{b^2 + 4D^{*2}}\right). \tag{3.9}$$

After organization, the time-varying quasi-steady lift becomes

$$C_{L_q} \propto \beta\Gamma^*_{0,\infty} - \frac{\beta^2 \Gamma^{*2}_{0,\infty} D^*}{\pi(b^2 + 4D^{*2})}. \tag{3.10}$$

According to thin airfoil theory, the coefficient of the first term is 2, which gives

$$C_{L_q} = 2\beta\Gamma^*_{0,\infty} - c_1 \frac{\beta^2 \Gamma^{*2}_{0,\infty} D^*}{\pi(b^2 + 4D^{*2})}, \tag{3.11}$$

where c_1 needs to be determined.

As an important side note, this formula can be used to determine a lift scaling relation for steady ground effect by neglecting the rotational lift or virtual camber term ($\dot{\theta}$ term) in $\Gamma^*_{0,\infty}$. Then a scaling law for steady ground effect can be deduced as

$$C_L^{steady} = 2\pi\beta\theta - c_1\frac{\pi\beta^2\theta^2 D^*}{b^2+4D^{*2}} \quad \text{where } c_1 = 2.76. \tag{3.12}$$

Using the static foil numerical and experimental data from figure 8(a), the coefficient is determined to be $c_1 = 2.76$ by linear regression. Figure 11(a) then compares the scaling law prediction with the data, which shows that it can predict the steady ground effect data to within 10 % for the numerical data and 15 % for the experimental data.

Returning to the time-varying formula (3.11), we can also consider an unsteady ground effect case where the foil undergoes sinusoidal pitching. If this scaling relation is then time averaged only a contribution from the second term will remain as

$$\bar{C}_{L_q} = -c_1\frac{\beta^2\overline{\Gamma^{*2}_{0,\infty}}D^*}{\pi(b^2+4D^{*2})}. \tag{3.13}$$

Considering that $\theta = \theta_0\sin(2\pi ft)$ and $\theta_0 = A^*/2 = St/(2k)$ we have

$$\bar{C}_{L_q} = c_1\phi_1, \tag{3.14}$$

$$\phi_1 = -\frac{\pi^3}{8}\left(\frac{\beta^2 D^*}{b^2+4D^{*2}}\right)\left(\frac{9}{4}+\frac{1}{\pi^2k^2}\right)St^2. \tag{3.15}$$

The coefficient $c_1 = 2.76$ determined from the static foil data is used for scaling the quasi-steady lift of both the steady and unsteady foil cases. Figure 11(b) presents an excellent collapse of the quasi-steady lift data over a wide range of St, k and D^*.

3.6.2. *Wake-induced lift*

The wake-induced lift can be calculated as

$$C_{L_w} \propto U^*\gamma\Gamma^*_{w,\infty}, \tag{3.16}$$

$$U^* = 1 + U^*_{i,1} + U^*_{i,2}, \tag{3.17}$$

where $\Gamma^*_{w,\infty}$ is the normalized infinite domain wake circulation, and the effective flow velocity U^* is composed of the velocity $U^*_{i,1}$, induced by an image bound vortex (representing the total bound vorticity, not the quasi-steady bound vorticity), and the velocity induced by an image wake vortex, $U^*_{i,2}$. To determine a scaling law for the wake-induced lift, consider a simplified flow model where a wake vortex is placed along the chord line at a distance of $U_\infty/(4f)$ downstream of the trailing edge (figure 11c), which gives,

$$U^*_{i,1} = \frac{-\Gamma^*_\infty\gamma}{\pi}\left(\frac{D^*}{b^2+4D^{*2}}\right) \quad \text{and} \quad U^*_{i,2} = \frac{-\Gamma^*_{w,\infty}\gamma}{\pi}\left[\frac{16k^2D^*}{(1+4k)^2+64k^2D^{*2}}\right], \tag{3.18a,b}$$

where Γ^*_∞ is the normalized infinite domain total circulation, and γ is the wake circulation amplification factor. By enforcing the Kutta condition at the foil's trailing edge, the wake

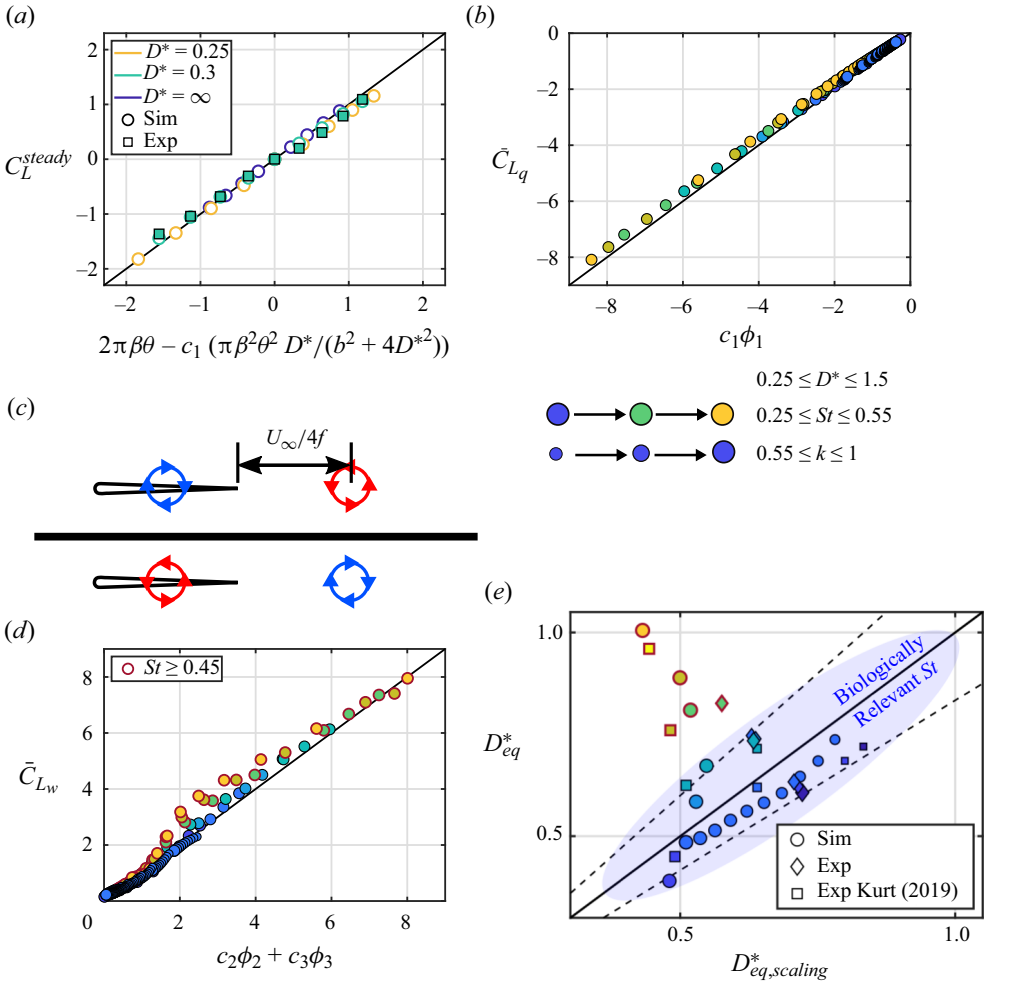

Figure 11. Scaling laws for steady and unsteady ground effects show a good collapse across a wide range of St, k and D^*. (*a*) The lift for a steady foil in ground effect (data from figure 8(*a*) with additional numerical case at $D^* = 0.25$) is compared with the steady foil scaling law. (*b*) The quasi-steady lift of an unsteady pitching foil (data from figure 9 compared with its scaling relation for $0.25 \le D^* \le 1.5$, $0.25 \le St \le 0.55$ and $0.55 \le k \le 1$. The marker colour from dark blue to light yellow represents increasing St while the marker size from small to large represents increasing k. (*c*) Schematic to illustrate the simple flow model for calculating the wake circulation amplification factor. (*d*) The wake-induced lift of an unsteady pitching foil compared with its scaling relation. Markers outlined in red represent data with $St \ge 0.45$. (*e*) Stable equilibrium altitudes compared with the scaling relation. Dashed lines present 20 % margins of error. These include 2-D numerical data with $0.25 \le St \le 0.55$ and $0.55 \le k \le 1$, and 2-D experimental data with $0.2 \le St \le 0.4$ and $0.6 \le k \le 0.9$, as well as 2-D experimental data from Kurt *et al.* (2019) with $0.2 \le St \le 0.6$ and $0.5 \le k \le 1$. Data points in the blue shaded area cover the Strouhal number range of biological locomotion (Taylor, Nudds & Thomas 2003; Saadat *et al.* 2017).

circulation amplification factor is calculated as

$$\gamma = \frac{1 + 4k(1-b)}{1 + 4k(1-b) - \dfrac{(1-b)^2}{(1-b)^2 + 4D^{*2}} - \dfrac{4k(1-b)}{1 + 64k^2D^{*2}}}. \tag{3.19}$$

Following Moored & Quinn (2018), we have

$$\Gamma^*_{w,\infty} \propto \Gamma^*_{0,\infty}\frac{k^*}{k^*+1} \quad \text{and} \quad k^* = \frac{k}{1+4St^2}, \tag{3.20a,b}$$

$$\Gamma^*_{\infty} \propto \Gamma^*_{0,\infty}. \tag{3.21}$$

Similar to the quasi-steady lift, after time averaging the wake-induced lift, only terms associated with $\Gamma^{*2}_{0,\infty}$ remain, which gives

$$\bar{C}_{L_w} = c_2\phi_2 + c_3\phi_3, \tag{3.22}$$

$$\phi_2 = -\gamma^2 St^2\left(\frac{9}{4}+\frac{1}{\pi^2k^2}\right)\left(\frac{D^*}{b^2+4D^{*2}}\right)\left(\frac{k^*}{k^*+1}\right), \tag{3.23}$$

$$\phi_3 = -\gamma^2 St^2\left(\frac{9}{4}+\frac{1}{\pi^2k^2}\right)\left[\frac{16k^2D^*}{(1+4k)^2+64k^2D^{*2}}\right]\left(\frac{k^*}{k^*+1}\right)^2. \tag{3.24}$$

By using the wake-induced lift data from figure 4, the coefficients were determined by linear regression to be $c_2 = -33.00$ and $c_3 = 83.35$. Figure 11(*d*) shows that a good collapse of the data can be achieved with the exception of data with $St \geq 0.45$ (outlined in red). As shown in figure 7(*a*), the wake-induced lift is significantly altered by a wake instability effect that occurs when $St \geq 0.45$ even for out-of-ground effect foils. Since this wake instability effect is not accounted for in the scaling laws, the data points with $St \geq 0.45$ (figure 11*d*) begin to show deviation from the scaling law prediction. Details of the scaling laws derivation, such as calculation of circulation amplification factors, velocities induced by the image system and time-averaged circulation square, can be found in Appendix A.

3.6.3. *Total lift*

Now, the quasi-steady lift and wake-induced lift can be summed to acquire the total lift, and the total lift becomes a function of St, k and D^*

$$\bar{C}_L = c_1\phi_1 + c_2\phi_2 + c_3\phi_3 = f\left(St, k, D^*\right). \tag{3.25}$$

Then, for a given pair of St and k, the equilibrium altitude, D^*_{eq}, can be determined by setting (3.25) to zero, which gives

$$c_1\frac{\pi^3}{8}\left(\frac{\beta^2}{b^2+4D^{*2}_{eq}}\right) + c_2\gamma^2\left(\frac{1}{b^2+4D^{*2}_{eq}}\right)\left(\frac{k^*}{k^*+1}\right) + c_3\gamma^2\left[\frac{16k^2}{(1+4k)^2+64k^2D^{*2}_{eq}}\right]\left(\frac{k^*}{k^*+1}\right)^2 = 0. \tag{3.26}$$

The equilibrium altitude cannot be written in a closed-form explicit solution, but rather (3.26) must be solved implicitly. In this way, (3.26) represents an implicit scaling law for the equilibrium altitude of a pitching foil in ground effect. Figure 11(*e*) presents the scaling law prediction for the equilibrium altitude. The scaling law can predict the equilibrium altitude to within 20 % error except for the data with $St \geq 0.45$. Moreover, the predicted equilibrium altitude for $St \geq 0.45$ is shown to decrease with increasing St. The deviation in the prediction of equilibrium altitudes at $St \geq 0.45$ is due to the deviation in

the wake-induced lift prediction, which is caused by neglecting the wake instability effect in the wake-induced lift scaling law. At $St \geq 0.45$ the foil has a non-zero time-averaged wake-induced lift as D^* goes to infinity. However, the time-averaged wake-induced lift always goes to zero in the scaling law as D^* goes to infinity. Data points in the blue shaded area in figure 11(*e*) cover the Strouhal number range of biological locomotion that is $0.2 \leq St \leq 0.4$ (Taylor *et al.* 2003; Saadat *et al.* 2017), so it can be observed that the scaling law captures the trend of the biologically relevant data. For the numerical data with $St < 0.45$ a 5 % and 10 % error in predicting the quasi-steady and wake-induced lift, respectively, leads to a 20 % error in predicting the equilibrium altitude. This indicates that the equilibrium altitude relies on a delicate balance and is sensitive to small changes in the lift components. This is also observed by Liu *et al.* (2023), who found that a pitch bias angle equal to 7 % of the amplitude can shift the equilibrium altitude of a pitching foil by 28 %.

4. Conclusions

In this article we decomposed the lift of a near-ground pitching hydrofoil into its added mass, wake-induced and quasi-steady components, and determined that their time-averaged values are always zero, positive and negative, respectively, across all ground proximities. This shows that both stable and unstable equilibrium altitudes are generated by a balance between positive wake-induced lift and negative quasi-steady lift while the added mass lift does not play a role.

Using both simulations and experiments, detailed analyses are provided to illustrate the three lift components' near-ground behaviour. In ground effect the negative peak of the added mass lift is amplified more than the positive peak, however, the negative peak also becomes sharper while the positive peak becomes broader compared with a foil out of ground effect. This leads to a scallop theorem result, where the added mass lift precisely integrates to zero over one oscillation cycle. Through a control volume analysis, the wake-induced lift is discovered to be positive due to the positive lift from the pressure difference on the control volume outweighing the negative lift from the net momentum flux. This leads to the upwards deflected wake behind a near-ground swimmer being responsible for a positive wake-induced lift. The quasi-steady lift is further analysed through the lens of the Kutta–Jowkouski theorem. It is observed that the velocity induced by the positive (negative) quasi-steady circulation bounded to the ground image foil enhances (reduces) the effective flow velocity at the foil's leading edge. For a pitching foil, this amplifies the negative quasi-steady lift during the upstroke and reduces the positive quasi-steady lift during the downstroke leading to a net negative quasi-steady lift. Additionally, the lift decomposition was applied to 3-D pitching foil simulations of varying aspect ratio. It was demonstrated that equilibrium altitudes of 3-D hydrofoils are also generated by a balance between positive wake-induced lift and negative quasi-steady lift. Moreover, as the aspect ratio decreases, the magnitude of the wake-induced lift drops off faster than the magnitude of the quasi-steady lift, leading to the disappearance of an equilibrium altitude when $\mathcal{AR} < 1.5$.

Using these insights, scaling laws of the quasi-steady lift, wake-induced lift and equilibrium altitudes are developed. Additionally, a simple scaling law for the lift of a steady foil in ground effect is discovered. The scaling laws show good agreement to both numerical and experimental data by predicting the equilibrium altitudes to within 20 % of their values as long as $St < 0.45$. For $St \geq 0.45$, significant effects from wake instability, not accounted for in the scaling laws, arise that alter the wake-induced lift. These results

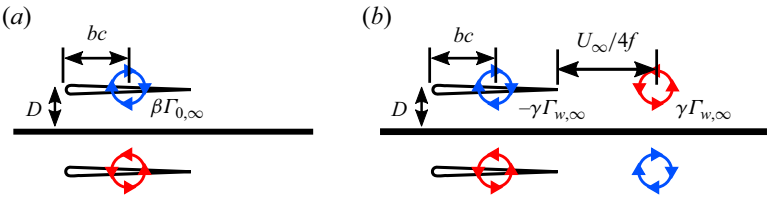

Figure 12. Schematics for calculating (a) the quasi-steady circulation amplification factor, β, and (b) the wake circulation amplification factor, γ.

not only provide key physical insights and scaling laws for unsteady ground effect, but also for two schooling hydrofoils in a side-by-side formation with an out-of-phase synchronization.

Funding. This work was supported by the National Science Foundation under Program Director Dr R. Joslin in Fluid Dynamics, award number 1921809 as well as by the Office of Naval Research under Program Director Dr R. Brizzolara on MURI grant number N00014-22-1-2616.

Declaration of interests. The authors report no conflict of interest.

Author ORCIDs.
Tianjun Han https://orcid.org/0000-0002-5319-123X;
Qiang Zhong https://orcid.org/0000-0002-8435-5938;
Amin Mivehchi https://orcid.org/0000-0002-9705-7972;
Daniel B. Quinn https://orcid.org/0000-0002-5835-5221;
Keith W. Moored https://orcid.org/0000-0002-4331-3774.

Appendix A. Derivation of scaling laws

A.1. *Quasi-steady circulation amplification factor*

When the foil is near the ground (figure 12a), in order for the Kutta condition to be preserved at the foil's trailing edge, an additional bound circulation of the real foil must arise to cancel the transverse velocity induced by the image foil, which gives

$$(\beta - 1)V_1 + V_2 = 0, \tag{A1}$$

with

$$V_1 = \frac{\Gamma_{0,\infty}}{2\pi(1-b)c} \quad \text{and} \quad V_2 = -\frac{\Gamma_{0,\infty}\beta}{2\pi}\left[\frac{(1-b)c}{(1-b)^2c^2 + 4D^2}\right], \tag{A2a,b}$$

where V_1 is the transverse velocity induced by the bound vortex of the real foil out of ground effect, and V_2 is the transverse velocity induced by the bound vortex of the image foil.

Then, $\Gamma_{0,\infty}/2\pi c$ can be divided from both sides, which gives

$$\frac{\beta - 1}{1-b} - \beta\left[\frac{(1-b)}{(1-b)^2 + 4D^{*2}}\right] = 0. \tag{A3}$$

After organization we have

$$\beta = 1 + \frac{(1-b)^2}{4D^{*2}}. \tag{A4}$$

A.2. *Wake circulation amplification factor*

When the foil is near the ground (figure 12*b*), in order for the Kutta condition to be preserved at the foil's trailing edge, additional bound and wake circulations of the real foil must arise to cancel transverse velocities induced by the image foil, which gives

$$(\gamma - 1)V_3 + (\gamma - 1)V_4 + V_5 + V_6 = 0, \tag{A5}$$

with

$$V_3 = \frac{\Gamma_{w,\infty}}{2\pi(1-b)c}, \quad V_4 = \frac{2\Gamma_{w,\infty} f}{\pi U_\infty}, \tag{A6a,b}$$

$$V_5 = -\frac{\Gamma_{w,\infty}\gamma(1-b)c}{2\pi[(1-b)^2c^2 + 4D^2]}, \quad \text{and} \quad V_6 = -\frac{2\Gamma_{w,\infty}\gamma f U_\infty}{\pi(U_\infty^2 + 64D^2f^2)}, \tag{A7a,b}$$

where V_3 and V_4 are transverse velocities induced by the bound and wake vortex of the real foil out of ground effect, and V_5 and V_6 are transverse velocities induced by the bound and wake vortex of the image foil.

Then $\Gamma_{w,\infty}/2\pi$ can be divided from both sides, which gives

$$\frac{\gamma - 1}{(1-b)c} + \frac{4f(\gamma - 1)}{U_\infty} - \frac{\gamma(1-b)c}{(1-b)^2c^2 + 4D^2} - \frac{4\gamma f U_\infty}{U_\infty^2 + 64D^2f^2} = 0. \tag{A8}$$

After organization we have

$$\gamma\left[\frac{1}{1-b} + 4k - \frac{1-b}{(1-b)^2 + 4D^{*2}} - \frac{4k}{1 + 64D^{*2}k^2}\right] = \frac{1}{1-b} + 4k. \tag{A9}$$

Then γ can be calculated as

$$\gamma = \frac{1 + 4k(1-b)}{1 + 4k(1-b) - \dfrac{(1-b)^2}{(1-b)^2 + 4D^{*2}} - \dfrac{4k(1-b)}{1 + 64k^2D^{*2}}}. \tag{A10}$$

A.3. *Calculation of time-averaged circulation square*

The normalized quasi-steady circulation is

$$\Gamma^*_{0,\infty} = \pi\theta + \frac{3\pi c\dot{\theta}}{4U_\infty} = \pi\theta_0 \sin(2\pi ft) + \frac{3\pi^2 cf\theta_0 \cos(2\pi ft)}{2U_\infty}, \tag{A11}$$

which, considering $\theta_0 = A^*/2 = St/(2k)$, becomes

$$\Gamma^*_{0,\infty} = \frac{\pi St}{2k}\sin(2\pi ft) + \frac{3\pi^2 St}{4}\cos(2\pi ft). \tag{A12}$$

The time-averaged square of the normalized quasi-steady circulation, $\overline{\Gamma^{*2}_{0,\infty}}$, is calculated as

$$\overline{\Gamma^{*2}_{0,\infty}} = f\int_0^{1/f}\left[\frac{\pi St}{2k}\sin(2\pi ft) + \frac{3\pi^2 St}{4}\cos(2\pi ft)\right]^2 \mathrm{d}t. \tag{A13}$$

After expansion we have

$$\overline{\Gamma^{*2}_{0,\infty}} = f\int_0^{1/f} \frac{\pi^2 St^2}{4k^2}\sin^2(2\pi ft) + \frac{3\pi^3 St^2}{4k}\sin(2\pi ft)\cos(2\pi ft) + \frac{9\pi^4 St^2}{16}\cos^2(2\pi ft)\,\mathrm{d}t. \tag{A14}$$

The second term in the above equation integrates to zero. Then we have

$$\overline{\Gamma^{*2}_{0,\infty}} = f\int_0^{1/f} \frac{\pi^2 St^2}{4k^2}\sin^2(2\pi ft) + \frac{9\pi^4 St^2}{16}\cos^2(2\pi ft)\,\mathrm{d}t = \frac{\pi^4 St^2}{8}\left(\frac{9}{4} + \frac{1}{\pi^2 k^2}\right). \tag{A15}$$

A.4. *Calculation of the induced flow velocity*

The horizontal velocity induced by an image bound circulation, Γ, at the foil's leading edge is calculated as

$$U_{i,1} = \frac{\Gamma}{2\pi\sqrt{b^2c^2 + 4D^2}}\left(\frac{2D}{\sqrt{b^2c^2 + 4D^2}}\right) = \frac{\Gamma D}{\pi(b^2c^2 + 4D^2)}. \tag{A16}$$

After normalization we have

$$U^*_{i,1} = \frac{\Gamma^*}{\pi}\left(\frac{D^*}{b^2 + 4D^{*2}}\right). \tag{A17}$$

The horizontal velocity induced by a image wake circulation, Γ, at the foil's leading edge is calculated as

$$\begin{aligned} U_{i,2} &= \frac{\Gamma}{2\pi\sqrt{4D^2 + \left(c + \dfrac{U_\infty}{4f}\right)^2}}\left(\frac{2D}{\sqrt{4D^2 + \left(c + \dfrac{U_\infty}{4f}\right)^2}}\right) \\ &= \frac{\Gamma D}{\pi\left[4D^2 + \left(c + \dfrac{U_\infty}{4f}\right)^2\right]}. \end{aligned} \tag{A18}$$

After normalization we have

$$U^*_{i,2} = \frac{\Gamma^*}{\pi}\left[\frac{16k^2 D^*}{(1+4k)^2 + 64k^2 D^{*2}}\right]. \tag{A19}$$

Note that Γ is a general representation for vortices at locations of the image bound or wake vortex, and it is replaced by circulations associated with $\Gamma_{0,\infty}$ or $\Gamma_{w,\infty}$ in the article accordingly.

References

Akoz, E., Mivehchi, A. & Moored, K.W. 2021 Intermittent unsteady propulsion with a combined heaving and pitching foil. *Phys. Rev. Fluids* **6** (4), 1–21.

BADDOO, P.J., KURT, M., AYTON, L.J. & MOORED, K.W. 2020 Exact solutions for ground effect. *J. Fluid Mech.* **891**, 1–13.

BAUDINETTE, R.V. & SCHMIDT-NIELSEN, K. 1974 Spatial heterogeneity and population stability evidence against a genetical component to performance on IQ tests. *Nature* **248**, 83–84.

BISPLINGHOFF, R.L., ASHLEY, H. & HALFMAN, R.L. 2013 *Aeroelasticity*. Courier Corporation.

BLAKE, B.Y.R.W. 1979 The energetics of hovering in the mandarin fish (Synchropus Picturatus). *J. Expl Biol.* **82** (1), 25–33.

BOSCHETTI, P.J., CÁRDENAS, E.M., AMERIO, A. & ARÉVALO, Á. 2010 Stability and performance of a light unmanned airplane in ground effect. In *48th AIAA Aerospace Sciences Meeting Including the New Horizons Forum and Aerospace Exposition*.

BRENNEN, C.E. 1982 A review of added mass and fluid inertial forces. *Tech. Rep.* Department of the Navy.

CLEAVER, D.J., WANG, Z. & GURSUL, I. 2012 Bifurcating flows of plunging aerofoils at high Strouhal numbers. *J. Fluid Mech.* **708**, 349–376.

COCHRAN-CARNEY, J.H. 2018 Free swimming bio-inspired hydrofoils in unsteady ground effect free swimming bio-inspired hydrofoils in. PhD thesis.

DAI, L., HE, G. & ZHANG, X. 2016 Self-propelled swimming of a flexible plunging foil near a solid wall. *Bioinspir. Biomim.* **11** (4).

DAS, A., SHUKLA, R.K. & GOVARDHAN, R.N. 2016 Existence of a sharp transition in the peak propulsive efficiency of a low-Re pitching foil. *J. Fluid Mech.* **800**, 307–326.

EMBLEMSVÅG, J.E., SUZUKIY, R. & CANDLERZ, G. 2002 Numerical simulation of flapping micro air vehicles. In *32nd AIAA Fluid Dynamics Conference and Exhibit*.

FERNÁNDEZ-PRATS, R., RASPA, V., THIRIA, B., HUERA-HUARTE, F. & GODOY-DIANA, R. 2015 Large-amplitude undulatory swimming near a wall. *Bioinspir. Biomim.* **10** (1),

GODOY-DIANA, R., AIDER, J.L. & WESFREID, J.E. 2008 Transitions in the wake of a flapping foil. *Phys. Rev.* E **77** (1), 1–5.

GRAHAM, W.R., PITT FORD, C.W. & BABINSKY, H. 2017 An impulse-based approach to estimating forces in unsteady flow. *J. Fluid Mech.* **815**, 60–76.

HAINSWORTH, F. 1988 Induced drag savings from ground effect and formation flight in brown pelicans. *J. Expl Biol.* **135**, 431–444.

HE, Y., QU, Q. & AGARWAL, R.K. 2015 Shape optimization of an airfoil in ground effect for application to WIG craft. In *53rd AIAA Aerospace Sciences Meeting 2014*.

IOSILEVSKII, G. 2008 Asymptotic theory of an oscillating wing section in weak ground effect. *Eur. J. Mech.* B/*Fluids* **27** (4), 477–490.

VON KÁRMÁN, T. & SEARS, W.R. 1938 Airfoil theory for non-uniform motion. *J. Aeronaut. Sci.* **5**, 379–390.

KATZ, J. 1985 Calculation of the aerodynamic forces on automotive lifting surfaces. *Trans. ASME J. Fluids Engng* **107** (4), 438–443.

KATZ, J. & PLOTKIN, A. 2005 *Low Speed Aerodynamics. From Wing Theory to Panel Methods*. Cambridge University Press.

KRASNY, R. 1986 Desingularization of periodic vortex sheet roll-up. *J. Comput. Phys.* **65** (2), 292–313.

KURT, M., COCHRAN-CARNEY, J., ZHONG, Q., MIVEHCHI, A., QUINN, D.B. & MOORED, K.W. 2019 Swimming freely near the ground leads to flow-mediated equilibrium altitudes. *J. Fluid Mech.* **875**, R1.

LEE, S.H. & LEE, J. 2011 Optimization of three-dimensional wings in ground effect using multiobjective genetic algorithm. *J. Aircraft* **48** (5), 1633–1645.

LIANG, C., OU, K., PREMASUTHAN, S., JAMESON, A. & WANG, Z.J. 2011 High-order accurate simulations of unsteady flow past plunging and pitching airfoils. *Comput. Fluids* **40** (1), 236–248.

LIU, L., ZHONG, Q., HAN, T., MOORED, K.W. & QUINN, D.B. 2023 Fine-tuning near-boundary swimming equilibria using asymmetric kinematics. *Bioinspir. Biomim.* **18** (1).

MARAIS, C., THIRIA, B., WESFREID, J.E. & GODOY-DIANA, R. 2012 Stabilizing effect of flexibility in the wake of a flapping foil. *J. Fluid Mech.* **710**, 659–669.

MCCUNE, J.E. & TAVARES, T.S. 1993 Perspective: unsteady wing theory – the Kármán/Sears theory. *Trans ASME J. Fluids Engng.* **115** (4), 548–560.

MIVEHCHI, A., DAHL, J. & LICHT, S. 2016 Heaving and pitching oscillating foil propulsion in ground effect. *J. Fluids Struct.* **63**, 174–187.

MIVEHCHI, A., ZHONG, Q., KURT, M., QUINN, D.B. & MOORED, K.W. 2021 Scaling laws for the propulsive performance of a purely pitching foil in ground effect. *J. Fluid Mech.* **919**, 1–13.

MOORED, K.W. 2018 Unsteady three-dimensional boundary element method for self-propelled bio-inspired locomotion. *Comput. Fluids* **167**, 324–340.

MOORED, K.W. & QUINN, D.B. 2018 Inviscid scaling laws of a self-propelled pitching airfoil. *AIAA J.* **57**, 1–15.

PARK, H. & CHOI, H. 2010 Aerodynamic characteristics of flying fish in gliding flight. *J. Expl Biol.* **213** (19), 3269–3279.

PARK, S.G., KIM, B. & SUNGA, H.J. 2017 Hydrodynamics of a self-propelled flexible fin near the ground. *Phys. Fluids* **29** (5).

PURCELL, E.M. 1977 Life at low Reynolds number. *Am. J. Phys.* **45** (1), 3–11.

QU, Q., LU, Z., GUO, H., LIU, P. & AGARWAL, R.K. 2015 Numerical investigation of the aerodynamics of a delta wing in ground effect. *J. Aircraft* **52** (1), 329–340.

QUINN, D.B., LAUDER, G.V. & SMITS, A.J. 2014*a* Flexible propulsors in ground effect. *Bioinspir. Biomim.* **9** (3).

QUINN, D.B., MOORED, K.W., DEWEY, P.A. & SMITS, A.J. 2014*b* Unsteady propulsion near a solid boundary. *J. Fluid Mech.* **742**, 152–170.

SAADAT, M., FISH, F.E., DOMEL, A.G., DI SANTO, V., LAUDER, G.V. & HAJ-HARIRI, H. 2017 On the rules for aquatic locomotion. *Phys. Rev. Fluids* **2** (8), 1–12.

TANDIDA, Y. 2001 Ground effect in flight. *JSME Intl J.* B **44** (4), 481–486.

TAYLOR, G.K., NUDDS, R.L. & THOMAS, A.L.R. 2003 Flying and swimming animals cruise at a Strouhal number tuned for high power efficiency. *Nature* **425** (6959), 705–707.

THEODORSEN, T. 1935 General theory of aerodynamic instability and the mechanism of flutter. *Tech. Rep.* 496 (originally ARR-1935). National Advisory Committee for Aeronautics.

TREMBLAY DIONNE, V. & LEE, T. 2018 Ground effect on the aerodynamics of a NACA 0015 airfoil with a plain trailing-edge flap. *Fluid Mech. Res. Intl J.* **2** (1), 1–7.

WEBB, P.W. 1993 the effect of solid and porous channel walls on steady swimming of steelhead trout oncorhynchus mykiss. *J. Expl Biol.* **178** (1), 97–108.

WEBB, P.W. 2002 Kinematics of plaice, Pleuronectes platessa, and cod, Gadus morhua, swimming near the bottom. *J. Expl Biol.* **205** (14), 2125–2134.

WIDNALL, S.E. & BARROWS, T.M. 1970 An analytic solution for two- and three-dimensional wings in ground effect. *J. Fluid Mech.* **41** (4), 769–792.

WU, J., SHU, C., ZHAO, N. & YAN, W. 2014 Fluid dynamics of flapping insect wing in ground effect. *J. Bionic Engng* **11** (1), 52–60.

YANG, W., LIN, F. & YANG, Z. 2010 Three-dimensional Ground Viscous Effect on Study of Wing-in- ground Effect. In *Proceedings of Third International Conference on Modelling and Simulation*, pp. 8–11.

YANG, Z., YANG, W. & LI, Y. 2009 Analysis of two configurations for a commercial WIG craft based on CFD. In *Collection of Technical Papers - AIAA Applied Aerodynamics Conference*.

YU, M.L., HU, H. & WANG, Z.J. 2012 Experimental and numerical investigations on the asymmetric wake vortex structures around an oscillating airfoil. In *50th AIAA Aerospace Sciences Meeting Including the New Horizons Forum and Aerospace Exposition*.

ZHONG, Q., HAN, T., MOORED, K.W. & QUINN, D.B. 2019 Aspect ratio affects the equilibrium altitude of near-ground swimmers. *J. Fluid Mech.* **917**, A36.

ZHU, Q., WOLFGANG, M.J., YUE, D.K.P. & TRIANTAFYLLOU, M.S. 2002 Three-dimensional flow structures and vorticity control in fish-like swimming. *J. Fluid Mech.* **468**, 1–28.

ZONG, Z., LIANG, H. & ZHOU, L. 2012 Lifting line theory for wing-in-ground effect in proximity to a free surface. *J. Engng Maths* **74** (1), 143–158.